https://doi.org/10.5194/egusphere-2025-1163
Preprint. Discussion started: 28 April 2025

Bayesian inversion of satellite altimetry for Arctic sea ice and snow thickness

Elie René-Bazin[1,2], Michel Tsamados[2], Sabrina Sofea Binti Aliff Raziuddin[2], Joel Perez Ferrer[2], Tudor Suciu[2], Carmen Nab[2,3], Chamkaur Ghag[4], Harry Heorton[2], Rosemary Willatt[2], Jack Landy[5], Matthew Fox[6], and Thomas Bodin[7]

[1]Département de Sciences de la Terre, Ecole Normale Supérieure de Lyon, Lyon, France
[2]Centre for Polar Observation and Modelling, Department of Earth Sciences, University College London, London, UK
[3]Ocean Forecasting Research & Development, Met Office, UK
[4]Department of Physics & Astronomy, University College London, London, UK
[5]Department of Physics and Technology, UiT The Arctic University of Norway, Tromsø, Norway
[6]Department of Earth Sciences, University College London, London, UK
[7]Institute of Marine Sciences (ICM-CSIC), Barcelona, Spain

Correspondence: Elie René-Bazin (elie.rene-bazin@ens-lyon.fr)

Abstract. Inverse methods have been widely used in the field of Earth Sciences, particularly in seismology. Here, we introduce a new application of inversion theory to retrieve Arctic sea ice thickness (SIT) and its overlying snow depth (SD) using freeboard data from Ku-band/Ka-band radar and laser altimeters. We do this using the TransTessellate2D algorithm, a Bayesian trans-dimensional approach that allows us to invert for an unknown number of model parameters. This new inversion method is probabilistic in nature, and can offer a novel understanding of covariances between fields of interest as well as their uncertainties. We use this approach to jointly retrieve SIT and SD in one step, without using a climatology for SD. The inversion results are statistically encouraging when compared to snow and ice evaluation products: for April 2019, we obtain a higher linear correlation coefficient and a slope closer to the one-to-one line than the AWI CryoSat-2 SIT product compared to the Operation Ice Bridge (OIB) SIT product. For the inverted SD, our results exhibit similar statistical properties to the UiT and AMSR2 SD products when regressed against the OIB SD product. The SD is similar in terms of spatial patterns to the AMSR2 product in the 2018-2021 winter periods. We evaluate the inversion against data from MOSAiC and IceBird missions. These evaluations are also promising, especially for IceBird. Using this approach, we can choose the number of physical variables (SIT, SD and penetration factors) to be inverted for. Thus, we can also invert for the penetration factor, either from one or both satellites (in addition to inverting for SIT and SD at the same time). This paves the way for further research in understanding these penetration factors and their link to SIT and SD retrievals. We obtain values for the penetration factors between 0.5 and 1.2 for CryoSat-2 and around 0 for ICESat-2. Lastly, we investigate the multi-frequency inversion using data from the Ka- and Ku-band radar altimeters, thus preparing for the European Space Agency's planned dual-frequency altimetry mission, CRISTAL.

1 Introduction

Over the past decades, climate change has had a significant impact on Earth and especially on polar regions such as the Arctic. In the Arctic Ocean, climate change has induced a decline in September sea ice of $12.8 \pm 2.3\%$ per decade from 1979 to 2018 (Pörtner et al., 2019). Sea ice has a major role in regulating Earth's climate by being involved in the exchanges of heat, moisture and momentum between the Arctic Ocean and the atmosphere. Sea ice is also important in regulating the global thermohaline circulation (Stroeve and Notz, 2018). As sea ice extent is declining, the sea ice thickness (SIT) and its overlying snow depth (SD) are thinning. Kwok (2018) found a decrease of 66% in mean SIT at the end of the melt season between 1958-1976 and the CryoSat-2 (2011-2018) period. Such a decrease is also observed for the SD. Webster et al. (2014) found a decrease of $37 \pm 29\%$ for SD in Western Arctic and $56 \pm 33\%$ over the Chukchi Sea between 2009-2013 compared to the Warren climatology (Warren et al., 1999). This climatology corresponds to SD measurements made between 1954-1991 at Soviet stations in the Arctic.

Monitoring SIT over time was only possible with ice-buoys and sonar instruments until the 1990s (Kwok and Rothrock, 2009). During the last two decades, important progress in radar and laser altimetry has made it possible to obtain pan-Arctic spatial and year-round temporal coverage (Landy et al., 2022) to estimate SIT and SD. Satellite altimeters are assumed to retrieve radar freeboards, height of the reflexion interface above sea level, from either the top of the snow or the top of the ice under conventional assumptions, by measuring the return travel time of the pulse.

Despite these improvements, altimeters do have some limitations. Firstly, the coverage depends on the satellite used. CryoSat-2, a Ku-band radar altimeter launched by the European Space Agency in April 2010, can reach 88°N while AltiKa, a radar altimeter using the less common Ka-band microwave band, can only reach 81.49°N. Measurements are made along-track, meaning that several orbits are necessary to obtain sufficient coverage of the Arctic, with standard products given as monthly averages on 25-50 km^2 grids. Recently, novel interpolation algorithms have been developed to compute continuous spatial maps of freeboards from the along track measurements, on shorter spatio-temporal scales (i.e. daily / 5 km^2) (Gregory et al. (2021), Gregory et al. (2024)). Another uncertainty comes from the estimation of the freeboard itself. It is commonly assumed that the laser pulse and Ka-band radar are reflecting at the snow-air interface whereas the Ku-band radar is reflecting at the snow-ice interface (Laxon et al. (2003), Guerreiro et al. (2016), Lawrence et al. (2018)). However, studies have shown that meteorological and snow geophysical properties could cause the Ku-band radar to be scattered at levels above the snow/ice interface (e.g., Willatt et al. (2011), Nandan et al. (2017), Nab et al. (2023)). A radar scattering bias that is unaccounted for would introduce a systematic bias in freeboard and derived SIT. To take this into account, we introduce a penetration factor (α), which is the assumed value for the fractional depth of the snowpack from which the laser and radar returns backscatter. If $\alpha = 1$, the pulse is scattering at the snow-ice interface (CryoSat-2 default assumption), while for $\alpha = 0$ the signal is coming from the snow-air interface (AltiKa, ICESat-2 (Ice, Cloud and Land Elevation Satellite) default assumption).

To deduce the SIT from the freeboards, the assumption of hydrostatic equilibrium needs to be made. To compute the SIT in this manner, estimates are required for the SD and ice and snow densities. Zygmuntowska et al. (2014) found that the uncertainty on SD could contribute up to 70% of the total laser altimetry thickness uncertainty. For the radar altimetry thickness uncertainty, others found that it could contribute up to 50% (Giles et al., 2007). The uncertainty on sea ice density could contribute up to 30-35 % (Zygmuntowska et al., 2014). See Landy et al. (2020) for a full uncertainty analysis.

Traditional approaches to compute satellite-derived SIT rely on the use of climatological values for SD. The Centre for Polar Observation and Modelling (CPOM; Tilling et al., 2018) and Alfred Wegener Institute (AWI; Hendricks et al., 2023) SIT and volume products are based on CryoSat-2 radar freeboard data (L1B SAR and SARIn mode). The former uses the Warren snow depth climatology (W99; Warren et al., 1999) directly, whilst the latter merges W99 with snow depth estimates from ASMR2 (Rostosky et al., 2018). The NASA product (Petty et al., 2023) uses ICESat-2 laser freeboard (ATL10) data, combined with NASA Eulerian Snow On Sea Ice Model (NESOSIM) snow loading to estimate SIT. These satellite-derived products all use additional auxiliary parameters such as mean sea surface height, sea ice concentration and sea ice type.

Alongside these products, methods have been developed to compute ice and snow thickness at the same time, without assumptions or climatology needed for the SD. Several studies suggest utilizing co-located satellites to derive SIT and SD from freeboard measurements under the assumption of hydrostatic equilibrium (Kwok and Markus, 2017; Kwok et al., 2020; Kacimi and Kwok, 2022). However, this latter approach requires the two satellites to have similar orbits, which is not the case most of the time. Another approach is to use the ratio between SD and SIT (Shi et al., 2020). This method shows promising results but other assumptions are made concerning the thermal state of ice and snow.

Inverse methods have the potential to account for new datasets to derive estimates of SIT while accounting for complexities and uncertainties (Tarantola, 2005). The inversion approach used here allows us to address some of the issues raised previously, namely the prescribed SD or collocation of the satellite data. The 2D trans-dimensional Bayesian method produces a probabilistic solution made of a large ensemble of models for SIT and SD, but also for penetration factors (α). With such a trans-dimensional approach, the dimension of the model space (map over the Arctic Ocean of SIT, SD and α) is an unknown during the inversion and depends on the density and uncertainty of the input data. The algorithm we use is adapted from the code presented in Hawkins et al. (2019a), previously used to compute a map of rates of relative sea level change (Hawkins et al., 2019b) and recently adapted for coastal SLR monitoring (Oelsmann et al., 2024). We first introduce the data used and the inverse method, before showing our results with different parametrizations. We compare these results with other products for ice and snow and some *in situ* measurements (MOSAiC). Finally, we discuss the shortcomings and potential of this method for data fusion of heterogeneous satellite input data in the context of the European Space Agency's (ESA) upcoming dual-frequency polar mission, CRISTAL (Copernicus Polar Ice and Snow Topography Altimeter).

2 Data

The data used for the inversion comes from CryoSat-2 (CS; L1B Baseline E), AltiKa (AK) and ICESat-2 (IS; ATL10 v6; Kwok et al., 2023b). These satellites were launched in 2010, 2013 and 2018, respectively. CS is a Ku-band radar altimeter, AK is a Ka-band radar altimeter and IS is a laser altimeter. We use the Lognormal Altimeter Retracker Model (LARM) processed dataset for CS and AK. This dataset uses a physical retracker approach to obtain a more accurate measurement of the freeboard, by incorporating a better understanding of the sea ice's large-scale roughness (Landy et al., 2020).

The inputs for the algorithm are two maps of freeboards from a combination of two satellites (either CS-IS or CS-AK). The input maps are obtained by binning 15 days (15th of the month ± 7 days) of along-track radar and laser freeboard data onto the 25 km EASE 2.0 grid for every month considered (Brodzik et al., 2012). Note that the data within the 15-day window are assumed equivalent in time. By using multiple days of data as input (especially with IS where clouds often obstruct data collection) we allow the algorithm to construct more cells. To optimize computational efficiency, the inversion was performed within this interval for each month. Extending the period would increase the volume of input data, thereby lengthening the inversion.

The accuracy of the inversion depends on uncertainties in the component datasets, and the weighting given to each freeboard measurement based on these uncertainties (e.g. Nab et al. (2025)):

- **CryoSat-2 and AltiKa:** To calculate the freeboard uncertainty for the binned radar freeboard data in each grid cell, we follow the methods of Landy et al. (2024). To start, we calculate the “single shot” range error for each grid cell: $0.1 \cdot (1/\sqrt{N})$ for CS SAR mode and $0.14 \cdot (1/\sqrt{N})$ for CS SARIn mode, based on Wingham et al. (2006), where N is the number of samples in each grid cell. For AK, based on Dettmering et al. (2015) : $0.05 \cdot (1/\sqrt{N})$. The SSHA uncertainty provided with the LARM data is then binned onto the 25 km EASE-2 grid, using the same method as the freeboard data. The range error and binned SSHA uncertainty are then used to calculate the freeboard uncertainty:

  $$FB_{unc}^{CS,AK} = \sqrt{(ssha\_unc \cdot \frac{1}{\sqrt{N_{tracks}}})^2 + range\_error^2} \tag{1}$$

  where N_{tracks} is the number of independent tracks used in the binning and $ssha\_unc$ is the binned SSHA uncertainty for each grid cell

- **ICESat-2:** The beam freeboard uncertainty provided with the IS data is binned onto the 25 km EASE-2 grid, using the same method as the freeboard data. The freeboard segment error is then calculated for each grid cell: $beam\_fb\_unc \cdot (1/\sqrt{N})$, where N is the number of samples in each grid cell. The laser freeboard uncertainty is then calculated as:

  $$FB_{unc}^{IS} = \sqrt{(ssha\_interpolation\_error \cdot (\frac{1}{\sqrt{N_{tracks}}})^2 + fb\_segment\_error^2} \tag{2}$$

  where N_{tracks} is the number of independent tracks used in the binning and $fb\_segment\_error$ is the binned beam freeboard uncertainty for each grid cell. An assumed value of 0.01 m is used for the SSHA interpolation error.

We compare the results from our inversion to the following SIT and SD products:

- **AWI:** SIT product from the AWI Helmholtz Center for Polar and Marine Research (Hendricks et al., 2023). The product is made over the Arctic Ocean for every month from October to April. The input data to compute the SIT is composed of radar measurements from CryoSat-2 and auxiliary data that includes some geophysical parameters (e.g. sea ice concentration, mean surface height).

https://doi.org/10.5194/egusphere-2025-1163
Preprint. Discussion started: 28 April 2025

- **AMSR2:** AMSR2 is a microwave radiometer working at a 89 GHz frequency, which follows AMSRE, that provides data on sea ice concentration, precipitations and other geophysical processes (Rostosky et al., 2018). Here, we use the AMSR2 product for SD.
- **OIB:** The Operation IceBridge campaign is a NASA program, aimed at improving our understanding of the processes occurring in the polar regions. We use the SD and SIT Quick-Look product (Kurtz et al., 2016). These data were created using measurements from a laser altimeter with a 1 m footprint (and wavelength of 532 nm) and simultaneously a radar altimeter. Assuming that the laser measures the total freeboard (ice freeboard and overlying snow) and that the radar reflects at the snow-ice interface, we can compute the SD and the SIT. The OIB measurements used here were taken in March and April, from 2011 - 2019. The snow depth data are binned onto the 25 km EASE-2 grid.
- **UiT:** Snow depth data derived from ICESat-2 and CryoSat-2, assuming radar penetration factors of 0 and 1, respectively, from Landy et al. (2024).
- **MOSAiC**: Expedition conducted during between October 2019-2020 by the research icebreaker R/V Polarstern across the central Arctic Ocean (Willatt et al. (2023), Nicolaus et al. (2022)).
- **IceBird**: SD from airborne radar of the AWI IceBird project. The measurements are base on the multi-sensor airborne data release and are available with (Jutila et al., 2021).

3 Methods

3.1 Forward model

The equations used for the forward model are obtained under the assumption of hydrostatic equilibrium (Forsström et al., 2011). They can be written as follows:

$$F_r^{cs} = \frac{\rho_w - \rho_i}{\rho_w} H_i + (1 - \alpha_{cs}\frac{c}{c_s} - \frac{\rho_s}{\rho_w}) H_s \tag{3}$$

$$F_r^{ak} = \frac{\rho_w - \rho_i}{\rho_w} H_i + (1 - \alpha_{ak}\frac{c}{c_s} - \frac{\rho_s}{\rho_w}) H_s \tag{4}$$

$$F_l^{is} = \frac{\rho_w - \rho_i}{\rho_w} H_i + (1 - \alpha_{is}\frac{c}{c_s} - \frac{\rho_s}{\rho_w}) H_s \tag{5}$$

where F_r^{cs}, F_r^{ak}, and F_l^{is} are the freeboards for CryoSat-2, AltiKa and ICESat-2, and ρ_w, ρ_i and ρ_s are the densities for sea water, sea ice and snow respectively. H_i is the SIT and H_s is the SD. c_s is the velocity of the radar pulse in the snow and c is

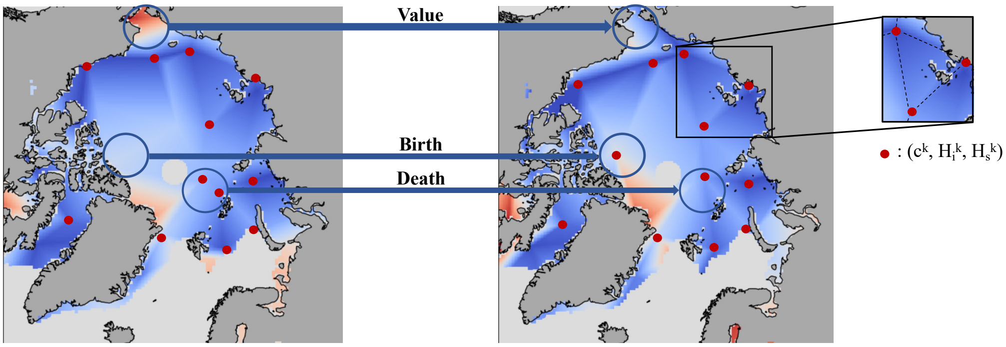

Figure 1. Schematic of 3 of the different perturbations than can be applied at each iteration of the algorithm. We display a zoom on a Delaunay triangle with the different model parameters associated to a node (red point). The red dots are the triangle vertices to which the parameter are associated and the dashed lines are the sides of the triangles.

the velocity in a vacuum. We assume that $\frac{c}{c_s} = 1.28$ (Kwok, 2014). α_{cs}, α_{ak} and α_{is} are the penetration factors for CS, AK and IS respectively. We use the sea ice type product from Aaboe et al. (2021) to classify each grid cell as first-year ice (FYI) or multi-year ice (MYI). We then assign sea ice bulk densities of 916.7 and 882 $kg \cdot m^{-3}$ for FYI and MYI, respectively, per Alexandrov et al. (2010). For sea water, we use $\rho_w = 1023\ kg \cdot m^{-3}$ (Wadhams et al., 1992). ρ_s evolves seasonally following Mallett et al. (2020):

$$\rho_s = 6.50M + 274.51 \tag{6}$$

where M is the number of months since October (i.e. $M = 3$ for January).

In order to formulate an inverse problem, we define a data vector **d**. We jointly invert a combination of CS and IS data (or CS and AK data), and define $\mathbf{d} = (\mathbf{d_{cs}}, \mathbf{d_{is}})$, with $\mathbf{d_{cs}} = \{(c^k_{cs}, F_r^{cs,k}), k \in [1, ..., N_{cs}]\}$, and $\mathbf{d_{is}} = \{(c^k_{is}, F_l^{is,k}), k \in [1, ..., N_{is}]\}$, and where c^k_{cs} are the coordinates of data of index k ($c^k_{cs} = (lon^k_{cs}, lat^k_{cs})$), $F_r^{cs,k}$ the value of the freeboards of index k, and N_{cs} the number of input data for CryoSat-2 (and same for IS).

3.2 Inverse modelling

A linear inverse problem is formulated following Tarantola (2005):

$$\mathbf{d} = \mathbf{Gm} + \epsilon \tag{7}$$

where **m** is the unknown model vector, **d** the data vector defined in 3.1, ϵ represents the data errors (i.e. the inability of the model to explain the data), and **G** is the forward model operator.

In order to parametrise the 2D maps of the variables to reconstruct (H_i, H_s and α), we use nodes and a Delaunay triangulation (Hawkins et al., 2019a). Here, the nodes of the Delaunay triangulation are unknown parameters, they are independent of the data locations and will randomly move during the inversion procedure. For our inversion, the vector $\mathbf{m}$ is defined as $\mathbf{m} = (\mathbf{m_{H_i}}, \mathbf{m_{H_s}})$ with (example for H_i) $\mathbf{m_{H_i}} = \{(c^k_{H_i}, H^k_i), k \in [1, ..., n_H]\}$ where $c^k_{H_i} = (lon^k_{H_i}, lat^k_{H_i})$ are the 2D coordinates of the node associated with index k (Figure 1), H^k_i the value for SIT associated to the node of index k, and n_H the number of nodes. The model vector $\mathbf{m_{H_s}}$ is defined in a similar way. We also invert for the penetration factor, and can thus write the vector model $\mathbf{m} = (\mathbf{m_{H_i}}, \mathbf{m_{H_s}}, \mathbf{m}_{\alpha_{\mathbf{cs,is}}})$ The three nodes defining each Delaunay triangle can be linearly interpolated to any point within the triangle by computing Barycentric coordinates (Sambridge et al., 1995). This then provides a continuous field over the domain but with discontinuities in the gradient at triangle edges.

Here, the dimension of the model space (the number of nodes n_{H_i}) will be treated as an unknown variable to be inverted for. In this way, the level of spatial resolution is directly determined by the data without having to define a smoothing parameter. We summarize the model and data vectors in Table 1.

Inversion name	Satellites	Data space	Model space
CS-IS-2p	CryoSat-2 / ICESat-2	$\mathbf{d_{cs}}, \mathbf{d_{is}}$	$\mathbf{m_{H_i}}, \mathbf{m_{H_s}}$
CS-IS-3p	CryoSat-2 / ICESat-2	$\mathbf{d_{cs}}, \mathbf{d_{is}}$	$\mathbf{m_{H_i}}, \mathbf{m_{H_s}}, \mathbf{m}_{\alpha_{\mathbf{cs}}}$
CS-IS-4p	CryoSat-2 / ICESat-2	$\mathbf{d_{cs}}, \mathbf{d_{is}}$	$\mathbf{m_{H_i}}, \mathbf{m_{H_s}}, \mathbf{m}_{\alpha_{\mathbf{cs}}}, \mathbf{m}_{\alpha_{\mathbf{is}}}$
CS-AK-2p	CryoSat-2 / AltiKa	$\mathbf{d_{cs}}, \mathbf{d_{ak}}$	$\mathbf{m_{H_i}}, \mathbf{m_{H_s}}$

Table 1. Summary table for the setups tested. The data vectors corresponds to the input of the algorithm and the output is a probability distribution in the model space.

In order to recover the model parameters from the observed data, we use a Bayesian approach, where all quantities are defined probabilistically:

$$P(\mathbf{m}|\mathbf{d}) = \frac{P(\mathbf{d}|\mathbf{m})P(\mathbf{m})}{P(\mathbf{d})} \tag{8}$$

where $P(\mathbf{d}|\mathbf{m})$ is the likelihood function representing the probability of observing the data given a particular model, $P(\mathbf{m})$ is the prior probability which represents the information we know on the model before measuring the data **d** (Bodin and Sambridge, 2009) and $P(\mathbf{d})$ can be seen as a normalization constant. The solution is $P(\mathbf{m}|\mathbf{d})$ and called the posterior probability distribution.

We use uniform prior distributions. For a given model parameter x, the prior distribution is:

$$P(x) = \begin{cases} \frac{1}{b-a}, & \text{if } a \le x \le b, \\ 0, & \text{else}, \end{cases} \qquad x \in \{H_i, H_s, \alpha_{cs}, \alpha_{is}\}. \tag{9}$$

The intervals $[a, b]$ for each distribution are as follows:

- H_i: $[0, 6]$ m
- H_s: $[0, 0.5]$ m

https://doi.org/10.5194/egusphere-2025-1163
Preprint. Discussion started: 28 April 2025

- α_{cs}: $[-0.5, 1.5]$
- α_{is}: $[-0.5, 0.5]$

We choose wide intervals for α_{cs} and α_{is} to allow a large degree of freedom to the method (even if a negative penetration factor doesn't have a physical meaning).

The likelihood function is based on a mathematical model for data errors. We make the assumption that the noise on the data is a combination of several sources of uncorrelated errors, such that the final distribution should converge towards a Gaussian as per the Central Limit Theorem. Furthermore, we use diagonal covariance matrices for simplicity (Hawkins et al., 2019a). Thus, the joint likelihood function is a Gaussian likelihood that can be written as

$$P(\mathbf{d}|\mathbf{m}) = P(\mathbf{d_{cs}}, \mathbf{d_{is}}|\mathbf{m}) = P(\mathbf{d_{cs}}|\mathbf{m}) \times P(\mathbf{d_{is}}|\mathbf{m}) = \frac{1}{\sqrt{2\pi}\sigma_{F^r_{cs}}\sigma_{F^l_{is}}} \exp\left(-\frac{\|g(\mathbf{m}) - \mathbf{d_{cs}}\|^2}{2\sigma^2_{F^{cs}_r}} - \frac{\|g(\mathbf{m}) - \mathbf{d_{is}}\|^2}{2\sigma^2_{F^{is}_l}}\right) \tag{10}$$

with $\sigma_{F^{cs}_r}$ and $\sigma_{F^{is}_l}$ being the standard deviations of the input data.

To estimate the posterior solution $P(\mathbf{m}|\mathbf{d})$, we use the reversible-jump algorithm (Green, 1995), which is an extension of the standard McMC Metropolis algorithm to models with variable levels of complexity. The algorithm produces a chain of random Delaunay models where each new proposed model is drawn as a random perturbation of the current model. The proposed model is either accepted or rejected according to an acceptance rule based on the ratio of posteriors probability of the current and proposed model. The solution thus obtained is a large ensemble of Delaunay models representing the posterior distribution.

At each iteration of the random walk, the algorithm makes a random choice between four perturbations of the model parameters (example for inversion of H_i and H_s only):

- **Value:** The value of a randomly chosen node of index k in the map is perturbed as well as its associated values H_i^k and H_s^k .
- **Birth:** A new node is created with the associated values randomly drawn from the prior distribution defined previously. That is, a new node is created with position $c_{H_i}^{n_H+1}$, and values $H_i^{n_H+1}$ and $H_s^{n_H+1}$.
- **Death:** A randomly chosen cell and the associated value of the physical parameter are deleted.
- **Move:** The position of a randomly chosen cell is perturbed (we perturb $c_{H_i}^k$).

These perturbations are illustrated in Figure 1. The random perturbations are drawn from a Gaussian distribution centered on the value of the model parameter and with a specified standard deviation.

We ran the algorithm with 1,500,000 iterations, and removed the first 500,000 models that form the "burn in" stage of the inversion (Brooks et al., 2011). Instead of looking at each of the remaining 1,000,000 models, we compute the mean over the ensemble by taking the average of all sampled values at each pixel. Since individual models have different parameterisations, this results in a smooth continuous map. The standard deviation over the ensemble can also be computed, thus providing a continuous error map. Note that other ways to exploit the information contained in the ensemble are available, such as taking a median, or maximum of the distribution at each geographical location.

https://doi.org/10.5194/egusphere-2025-1163
Preprint. Discussion started: 28 April 2025

4 Results

4.1 Inversion for SIT and SD, without assumptions on penetration factors

Arctic maps of SIT and SD are computed for every winter from 2018 to 2021 using freeboards from a combination of either CryoSat-2/ICESat-2 (CS-IS) or CryoSat-2/AltiKa (CS-AK). The resulting SIT and SD maps with the two combinations of satellites are presented in Figure 2 and 4, for prescribed values of $\alpha_{cs} = 1$ and $\alpha_{is} = 0$. The lack of data near the pole for CS-AK comes from AltiKa's orbit, limited to 81.49°N.

4.1.1 Sea ice thickness (SIT)

In the CS-IS inversion we observe an increase in SIT from November to April each year. We obtain thicker ice in the North of the Canadian Archipelago and in the Central Arctic (2.5 - 4 m) than in the rest of the Arctic Ocean (0 - 3 m). The CS-AK-2p inversion doesn't include the Central Arctic, but the SIT near the Canadian Archipelago is similar to that found in CS-IS (around 4 m). The observed spatial patterns are consistent with the ice type (MYI or FYI) patterns, with thicker ice found in regions typically dominated by MYI (north of Greenland and Canadian Archipelago). We find similar spatial distributions for the SIT between the two combinations used (CS-IS and CS-AK) which shows that the method appears to be robust and flexible towards the combination of satellites used.

When comparing the results of the inversion to the AWI SIT product, we observe the same spatial patterns for the ice around the Central Arctic. However, the values from the inversion are 0.5 - 1 m higher than the ones from AWI, especially to the north of Greenland. It is worth noting that our inversion results indicate thicker sea ice north of Greenland and in the Canadian Archipelago, while the AWI dataset generally shows greater ice thickness across the broader Arctic Ocean. This result can be confirmed looking at the maps for AWI (Figure 2, left column) in which we find a wider spread in the thick sea ice over the Arctic Ocean. For the inversion, the thicker sea ice remains contained in a specific area.

Next, we compare the results from the CS-IS model with estimates from airborne sensors retrieved during NASA's Operation Ice Bridge (OIB) campaign in April 2019 (Figure 3).

We find an improved linear correlation coefficient (r = 0.70), slope (nearly 1 for the inverse SIT) and lower intercept with the inverse solution compared to the AWI product. The Bias and RMSE are similar between both SIT products (Table 2). The inversion solution assuming α_{cs} = 1 underestimates the SIT by 18 cm; however, it represents the spread of thickness estimated by OIB better than the conventional AWI SIT product.

4.1.2 Snow depth (SD)

A main advantage of our method is being able to retrieve ice and snow thickness simultaneously. We retrieve the same spatial patterns for snow between CS-IS and AMSR2, especially over Central Arctic and in the Beaufort Sea (Figure 4). Again, the result with CS-AK is limited because of AltiKa's orbit. Compared to SIT shown in Figure 2, the snow inversion for CS-IS and CS-AK displays larger spatial differences. When looking at the difference between CS-IS and AMSR2, we see that the two

https://doi.org/10.5194/egusphere-2025-1163
Preprint. Discussion started: 28 April 2025

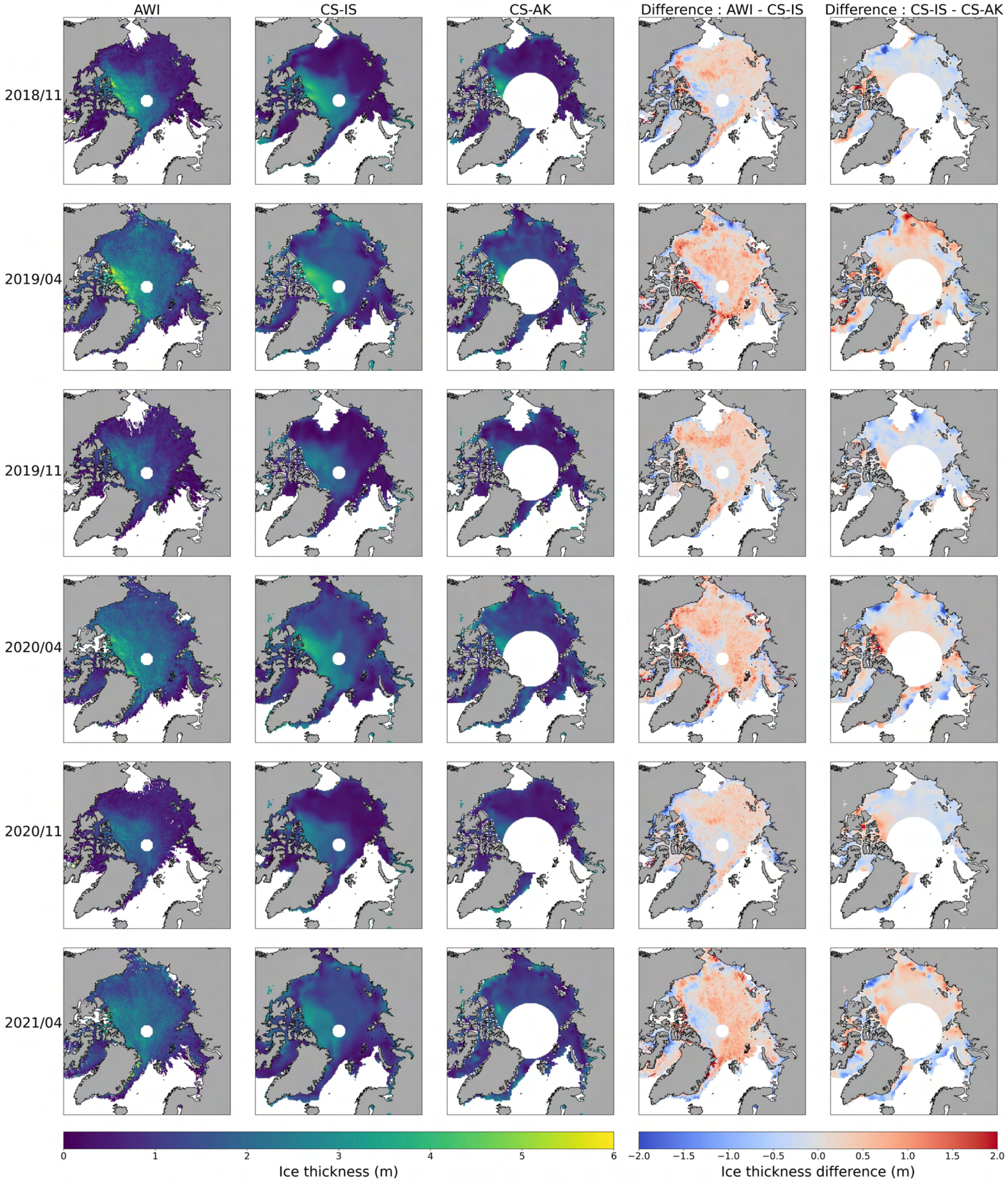

Figure 2. Results of the inversion for the SIT using CS-IS-2p and CS-AK-2p, with $\alpha_{cs} = 1$ and $\alpha_{is} = \alpha_{ak} = 0$. The first column shows the AWI SIT product, for visual comparison. The second and third columns show the CS-IS and CS-AK results, respectively. The fourth column shows the difference between the AWI product and the CS-IS results. The fifth column shows the difference in inversion results between the two satellite combinations (CS-IS and CS-AK).

https://doi.org/10.5194/egusphere-2025-1163
Preprint. Discussion started: 28 April 2025

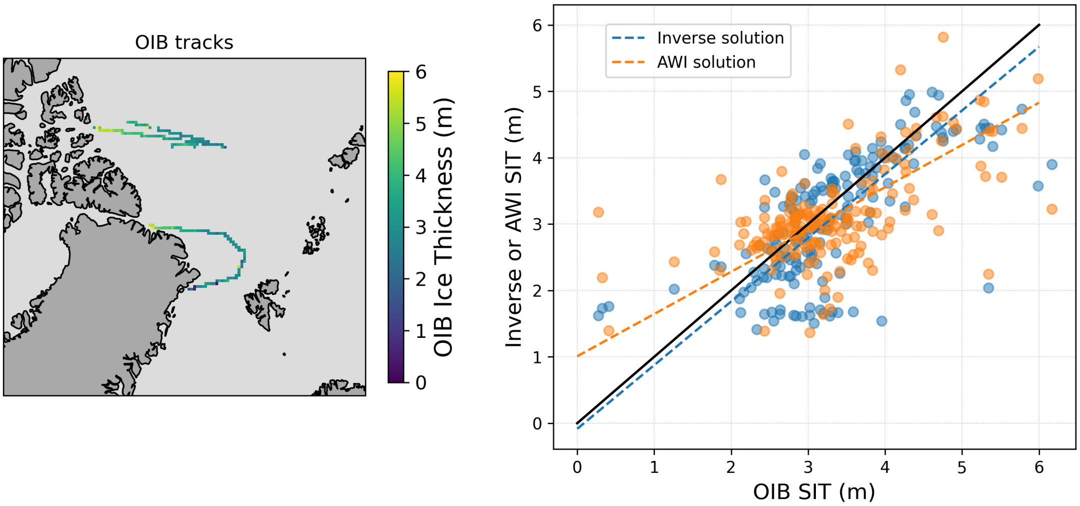

Figure 3. (left) Map of SIT retrieved from OIB tracks for April 2019. (right) Comparison of the CS-IS-2p SIT inversion and AWI SIT product with Operation Ice Bridge for April 2019. The dashed lines of best fit are computed using the orthogonal distance regression between the two sets of data (CS-IS-2p/OIB and AWI/OIB).

snow products are close (the difference being close to zero in a large part of the Arctic Ocean). The most important differences are located in the Beaufort Sea (November 2018) and in the Central Arctic (November 2019 and 2020). The AMSR2 snow depths have a stronger contrast between zones of first-year and multi-year ice, in comparison to the CS-IS SD. We can also notice that the differences between CS-IS and AMSR2 are generally higher in November than in April (and for April, the inverse SD is mostly higher than from AMSR2).

Figure 5 and Table 2 show a comparison of the CS-IS-2p inversion results against the OIB, AWI, UiT and AMSR2 SD products. The inversion method produces better results than the AWI product in terms of slope and linear correlation coefficient (r), whereas the values for the Bias, RMSE and intercept are similar. The inversion solution tends to overestimate low SD values and underestimate the high ones.

The inverse solution is non-biased ($Bias = 0.00$). The UiT product is statistically better than the inverse solution and the AWI product in terms of slope and intercept. Similar values for the bias, RMSE and linear correlation coefficient (r) are obtained between the inverse solution and UiT product. The SD from AWI is mainly centered around 0.35 cm for all the values plotted, which is a known issue of using the W99 climatology for MYI. Among all the datasets, AMSR2 is showing the best slope and intercept, which suggests that its stronger contrast of SD between FYI and MYI zones is more realistic.

However, the OIB snow product relies on radar penetrative assumptions as CS does (and also on snow density assumptions that might not be correct). If this product is biased, our comparison will be biased too. Thus, we perform some validations against measurements from MOSAiC and IceBird campaigns (Figure 6).

Similar to the comparison with OIB, the inverse solution for SD exhibits a bias and RMSE close to zero in both cases. The Pearson correlation coefficients obtained for these two validations are higher than those obtained when regressing against

https://doi.org/10.5194/egusphere-2025-1163
Preprint. Discussion started: 28 April 2025

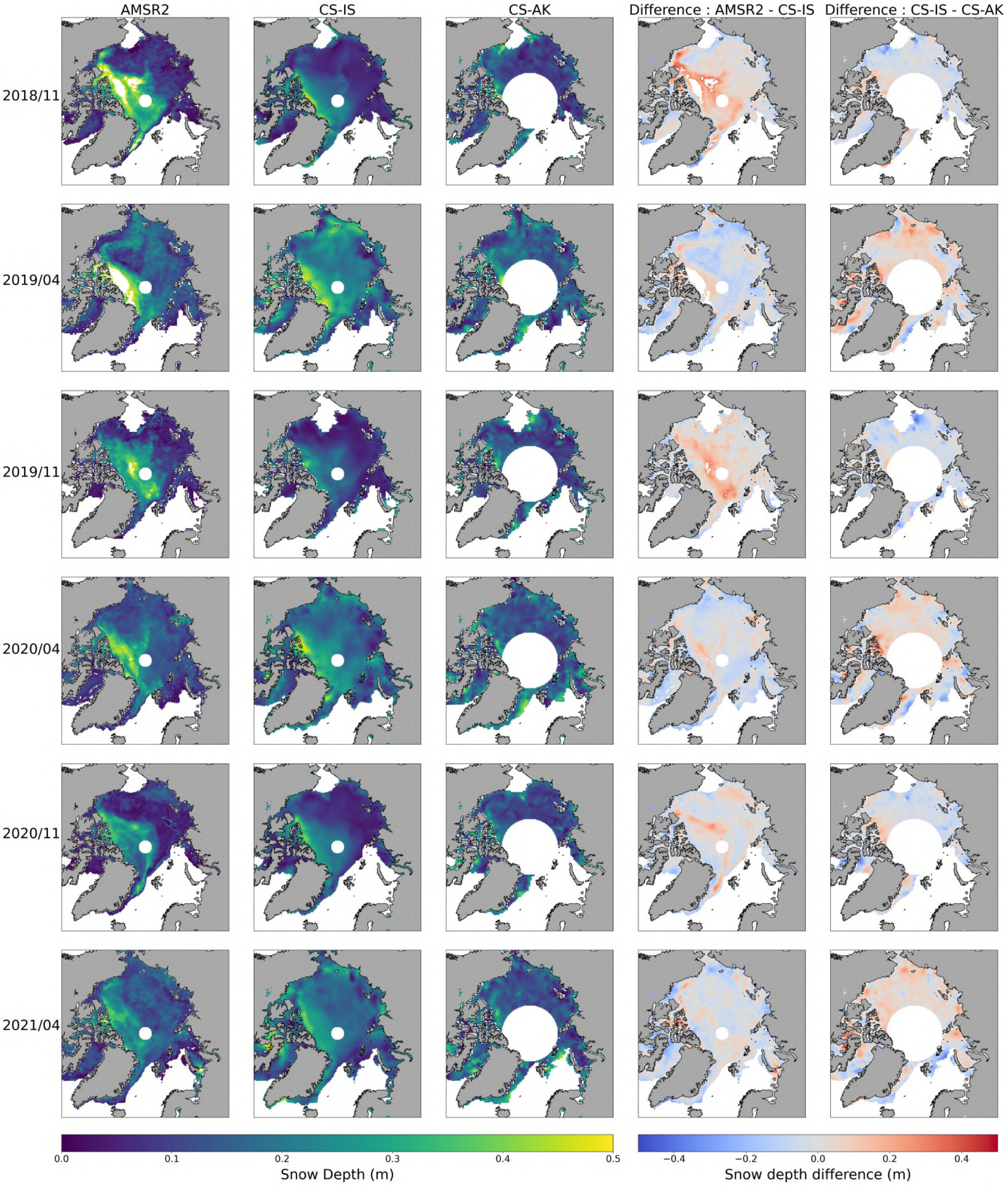

Figure 4. Comparison of our inversion for SD against AMSR2 product with $\alpha_{cs} = 1$ and $\alpha_{ak} = 0$. We also compute the difference between AMSR2 and the CS-IS combination and the difference between the two combinations of satellites.

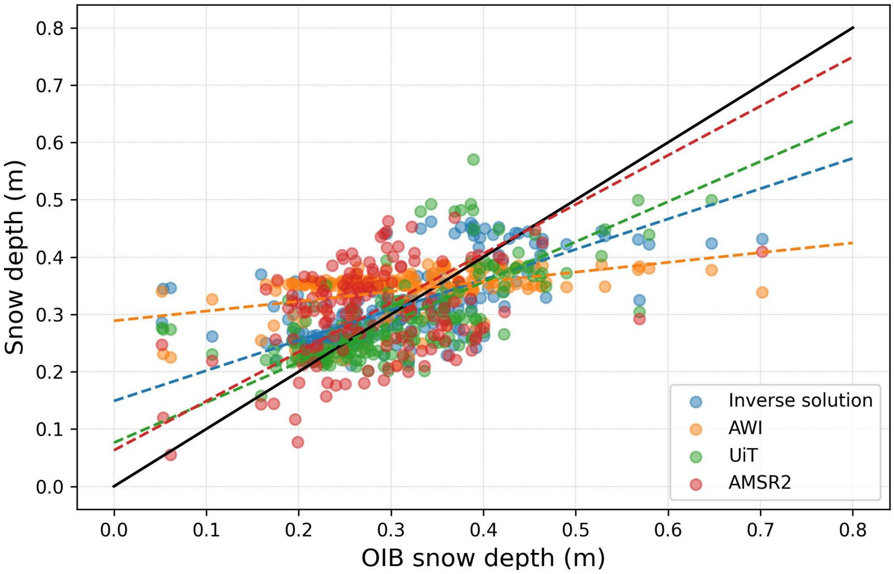

Figure 5. Evaluation of the result from the inversion using CS-IS-2p for snow depth. We compare our result with the OIB snow product, for April 2019. We also plot the snow used by AWI and the UiT and AMSR2 products.

	Inverse	**AWI**	**UiT**	**AMSR2**
Ice Thickness				
Bias	-0.21	-0.19	-	-
RMSE	0.74	0.79	-	-
r	0.70	0.61	-	-
Slope	0.99	0.64	-	-
Intercept	-0.18	1.01	-	-
Snow Depth				
Bias	0.00	0.03	-0.02	0.02
RMSE	0.08	0.10	0.07	0.10
r	0.63	0.37	0.68	0.34
Slope	0.53	0.17	0.70	0.86
Intercept	0.15	0.29	0.08	0.06

Table 2. Computed statistics corresponding to the Figure 3 and 5. The SD from AWI corresponds to the Warren Climatology.

OIB. When compared to MOSAiC, the inversion solution underestimates the SD by 19 cm. The derived slope (slope = 1.54) indicates that the inverse SD is underestimated for lower SD values and overestimated for higher SD values. The evaluation against IceBird yields near-perfect agreement, with a slope of 0.94. In this case, the inverse SD is overestimated by 3 cm.

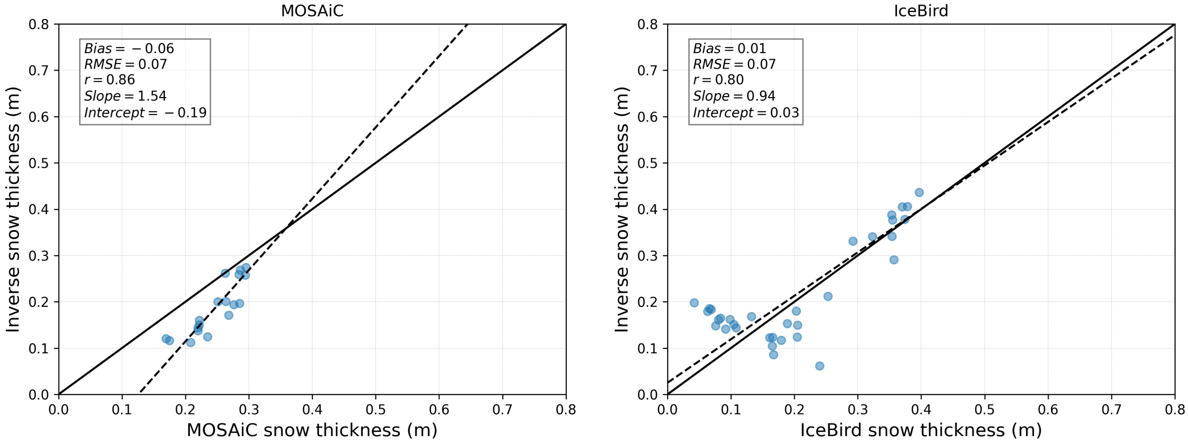

Figure 6. Evaluation of the results from the inversion using CS-IS-2p for SD. The validation is performed against MOSAiC (for Winter 2019-2020) and IceBird (for 2019/04).

Overall, the statistical performance against these measurements is improved compared to the validation against OIB (Table 2, Figure 5).

4.2 Inversion for SIT, SD and penetration factors

For the 3 (α_{cs}, SIT and SD) or 4 (α_{cs}, α_{is}, SIT and SD) variables inversions, we invert for the penetration factors in addition to the SIT and SD. The algorithm, using the defined prior distributions $P(m_{\alpha_{cs}})$ and $P(m_{\alpha_{is}})$, computes maps for each penetration factor (more details on the prior distributions can be found in Section 3).

In Figure 7, we find the results of the inversion for CS-IS-3p for winter 2020-2021 (every month from November to April). We find that both SD and SIT are increasing from November to April, even if the increase is less important for the SIT. We retrieve the expected spatial patterns for ice and snow (high SIT (2 - 4 m) and SD (> 0.4 m) north of Greenland). We find an asymmetry between West and East of Baffin Bay, with a higher SD on the West part of the bay, especially for April. On the maps for SIT, this asymmetry is less obvious, even if it is distinguishable for April. Looking at the maps for the penetration factor α_{cs}, the general patterns are close to full penetration (α_{cs} = 1) over MYI north of Greenland and Canada, and over FYI in the Arctic Ocean's marginal seas, but only partial penetration (α_{cs} between 0.5 and 0.75) over the second year ice in the Central Arctic. From November to April, the penetration factor maps are very similar. Some changes can be seen over the Canadian Archipelago and more generally on the borders of the Arctic Ocean.

There are some similarities when comparing the maps for α_{cs} and the results for SIT and SD. Especially for April, the penetration factor is important around Wrangel Island. In this same area, SIT is higher (close to 3 m). Similarly, on the north of Greenland where $\alpha_{cs} \simeq 1$, the SIT is important (around 4.5 m in some places) but here the SD is also important (even if we find a thinner ice close to the Canadian Archipelago).

As detailed in Section 3, the boundaries for the prior distribution on this penetration factor are [-0.5;1.5], with the range of values inverted for between 0.5 and 1.2 approximately. This suggests that the algorithm, using a prior with a great degree of freedom, is capable of retrieving values for α_{cs} that are similar to those in the literature, however, the range of values obtained for α is larger than found previously by Nab et al. (2023, 2024).

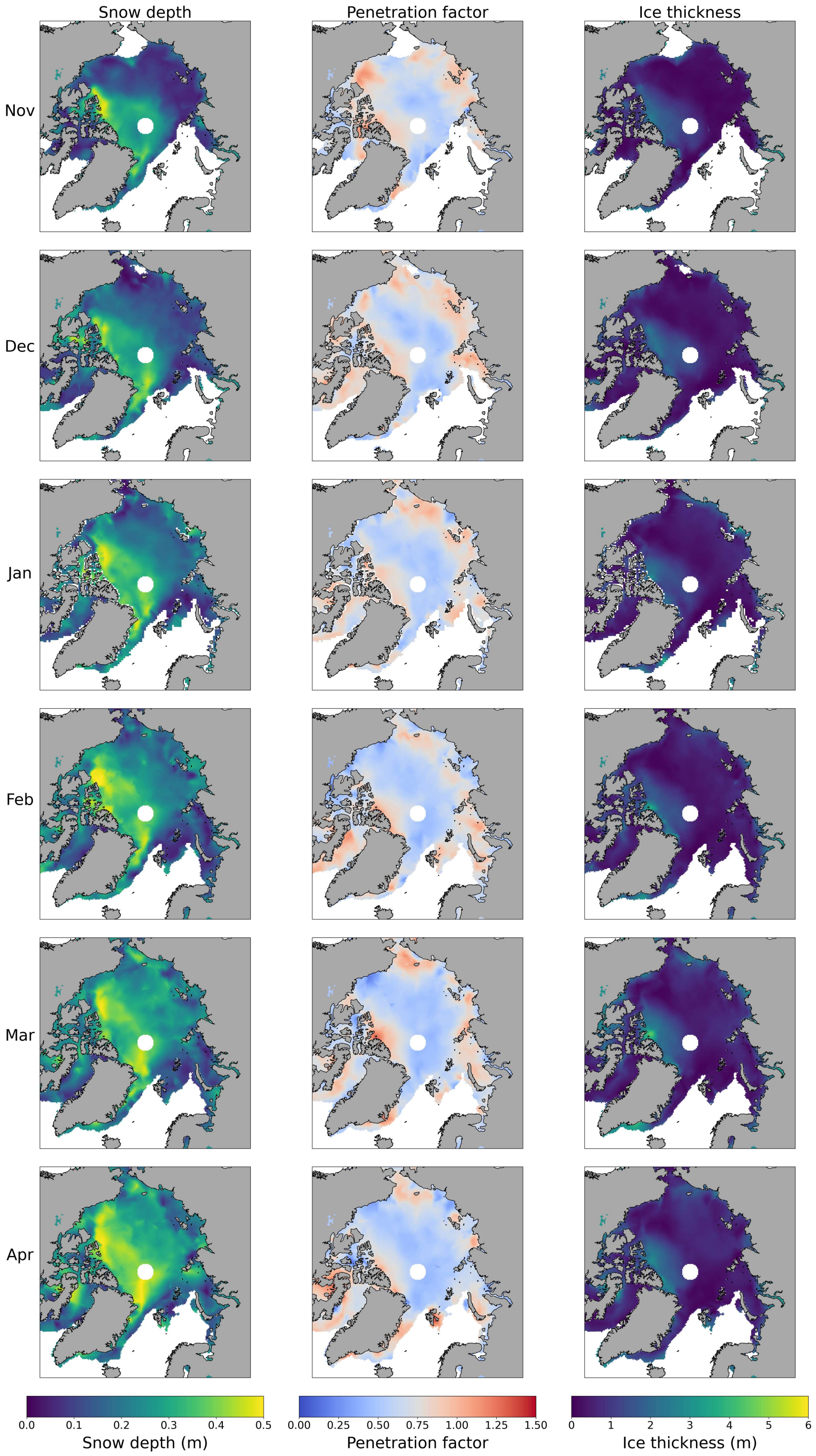

Figure 7. Inverse solution for CS-IS-3p for winter 2020-2021 (November to April). The inversion is performed for the (left column) SD, (middle column) penetration factor of CS and (right column) SIT. We assume $\alpha_{is} = 0$.

Focusing on month-to-month variability of α_{cs}, we plot the evolution of the average of this penetration factor over the Arctic Ocean of this penetration factor, for the same winter 2020-2021, on Figure 8. The penetration factor is slightly increasing between November and December (from ≈ 0.703 to 0.720). From December to April, α_{cs} is decreasing up to 0.67. This decreasing tendency can be observed on the maps on Figure 7, especially over Central Arctic and some borders of the Arctic Ocean. On Northern Alaska: penetration factor values > 0.75 in November and around 0.50 starting from January. Same observation for the borders of the Arctic Ocean close to Siberia.

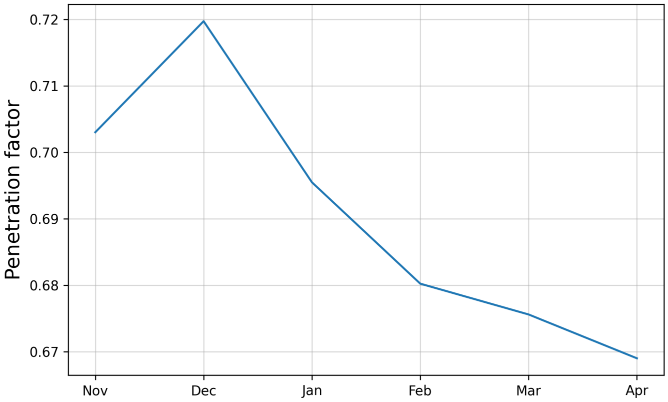

Figure 8. Pan-Arctic average of α_{cs} for Winter 2020-2021 (see Figure 7)

In Figure 9.(a), the CS-IS-3p SIT shows a better linear correlation coefficient against OIB than the AWI SIT product (r = 0.77 and 0.61, respectively) and the slope is closer to 1 than for AWI (slope = 1.31 and 0.64, respectively). However, the obtained bias and RMSE are worse for the inversion solution than for AWI. The bias is much larger for this model than for CS-IS-2p (see Table 2) which emphasizes the role of the penetration factor in the resulting SIT. This model exhibits a tendency to underestimate SIT, albeit to a lesser extent than observed in CS-IS-2p (Table 2). One possible explanation for this underestimation is a slight bias leading to underestimation in the freeboards measured by CS, IS, or both.

The inverted SD shown in Figure 9 compares very poorly with the OIB snow and with the other products tested (AWI, AMSR2 and UiT). The values obtained by our inversion (for the specific region of evaluation against OIB) are mainly grouped around 0.5 m and thus overestimate the SD compared to OIB. We find that the regions we used to compare with OIB (Central Arctic and Northeast of Greenland) are mainly regions where $\alpha_{cs} < 1$ (Figure 12). This result is consistent with the equations 3, 5 for prescribed freeboards and densities (decreasing the α_{cs} leads to an increase of H_s).

As performed for CS-IS-2p, we evaluate the CS-IS-3p SD against the MOSAiC and IceBird SD products, as shown in Figure 10. In contrast to the results obtained for CS-IS-2p (Figure 6) but similar to the evaluation against OIB SD, the CS-IS-3p model exhibits a systematic overestimation of SD in the region covered by MOSAiC, with most data points lying above the one-to-one line. This overestimation increases with SD, as indicated by the slope of 2.89. Analysing the mean α_{cs} for Winter 2019–2020 (Figure 11), we observe that the region corresponding to the MOSAiC comparison (Central Arctic, north of Svalbard; see Supplementary Information for the exact track locations) is characterized by a relatively low penetration factor

https://doi.org/10.5194/egusphere-2025-1163
Preprint. Discussion started: 28 April 2025

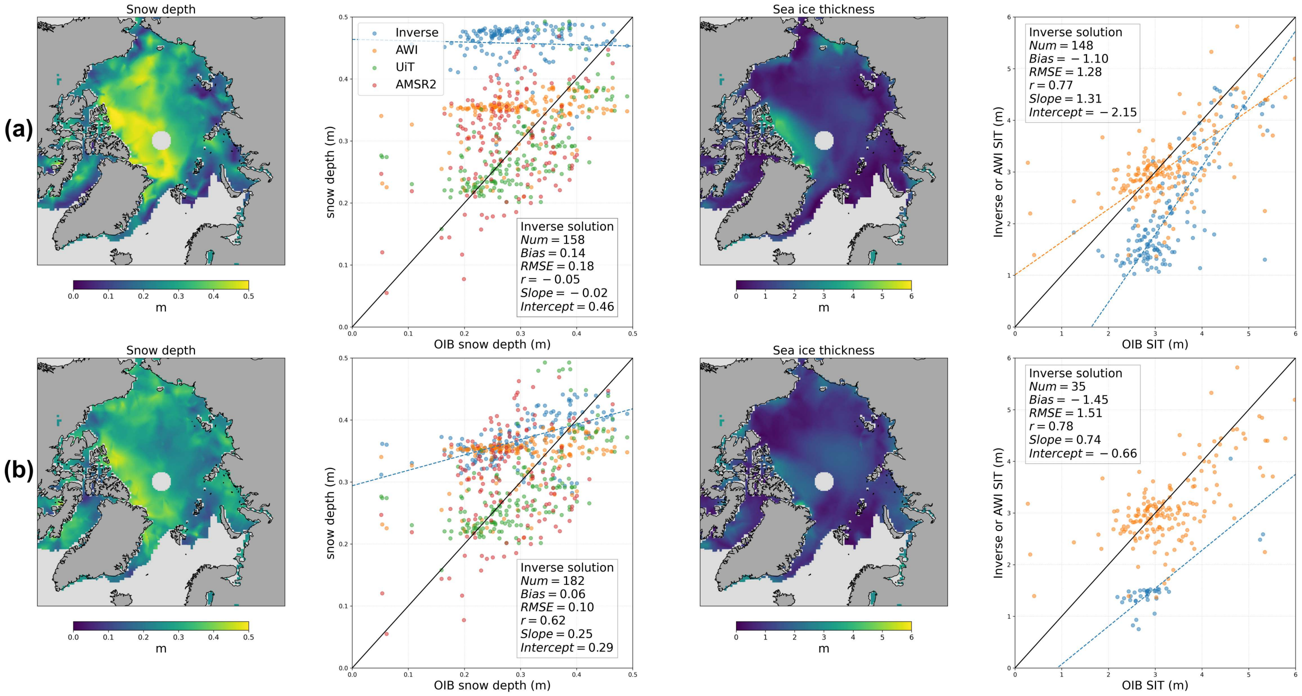

Figure 9. Comparison against OIB for (a) CS-IS-3p and (b) CS-IS-4p for April 2019. The comparison is made for (left column) SD and (right column) SIT.

(approximately 0.6). This is consistent with the observed SD overestimation, as a lower penetration factor for CS leads to increased SD estimates, in accordance with Equations 3 and 5.

In contrast, the comparison against IceBird (right plot) yields more favourable results, with a slope closer to unity (0.73) and reduced bias and RMSE compared to the MOSAiC validation. The regions covered by IceBird primarily encompass the marginal zones of the Arctic Ocean, including areas north of Canada and the Canadian Archipelago. These regions exhibit higher penetration factor values (Figure 12), which, according to the forward model equations (see Section 3.1), correspond to areas of lower SD.

Finally, we perform the inversion with both penetration factors as unknown (α_{cs} and α_{is}). The resulting maps for April 2019 are plotted in Figure 9.(b). Compared to the results from CS-IS-3p (Figure 9.(a)), we retrieve similar spatial patterns north of the Canadian Archipelago for the SIT. Likewise, the SD is similar in terms of spatial distribution. We retrieve small SDs to the north of Wrangel Island and thick snow over North Greenland (> 0.5 m). However, the SIT and SD obtained with CS-IS-4p are lower than the SIT and SD from CS-IS-3p. Looking at the maps for both penetration factors, it seems that α_{cs} is similar to that obtained with CS-IS-3p, even if, for CS-IS-3p, α_{cs} has a higher value over a large part of Central Arctic (around 0.6) and on the borders of the Arctic Ocean. We observe the same high values (> 1.2) on the north of Wrangel Island and the marginal seas. Globally, the penetration factor for CryoSat-2 computed with CS-IS-4p is lower than the one computed with CS-IS-3p.

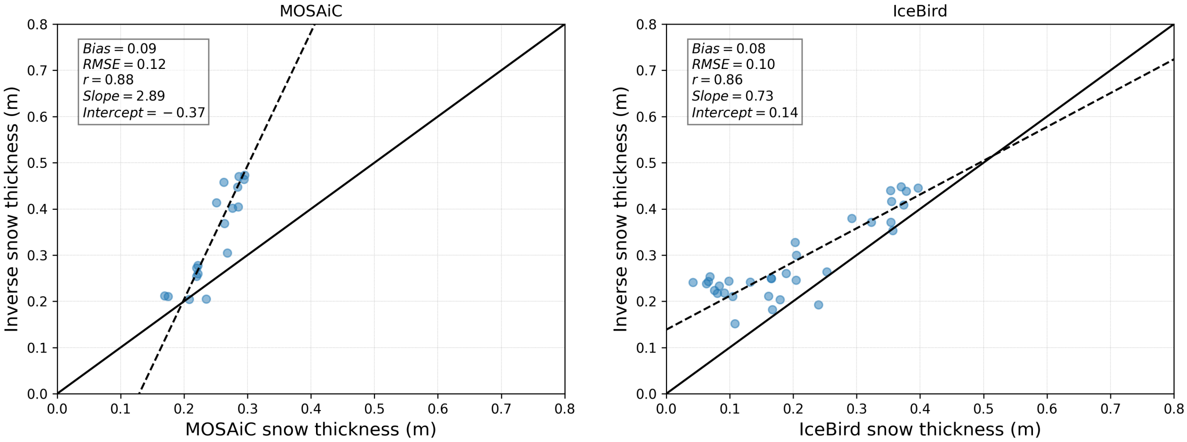

Figure 10. Evaluation of the results from the inversion using CS-IS-3p for SD. The validation is performed against MOSAiC (for Winter 2019-2020) and IceBird (for 2019/04).

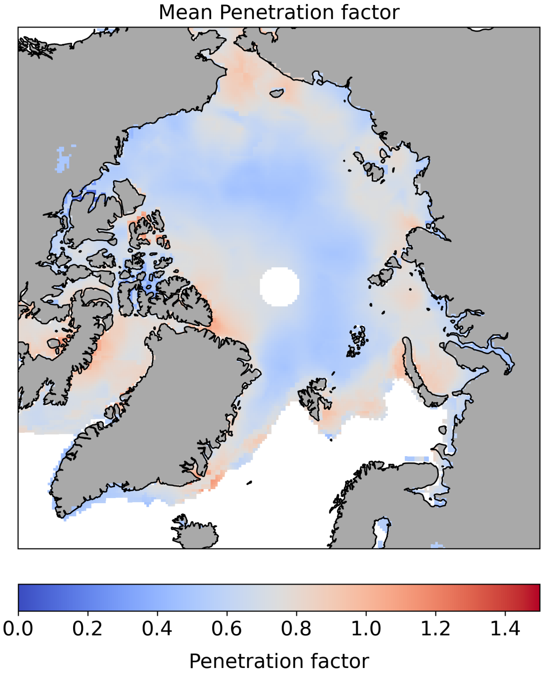

Figure 11. Mean penetration factor computed with CS-IS-3p model for Winter 2019-2020.

https://doi.org/10.5194/egusphere-2025-1163
Preprint. Discussion started: 28 April 2025

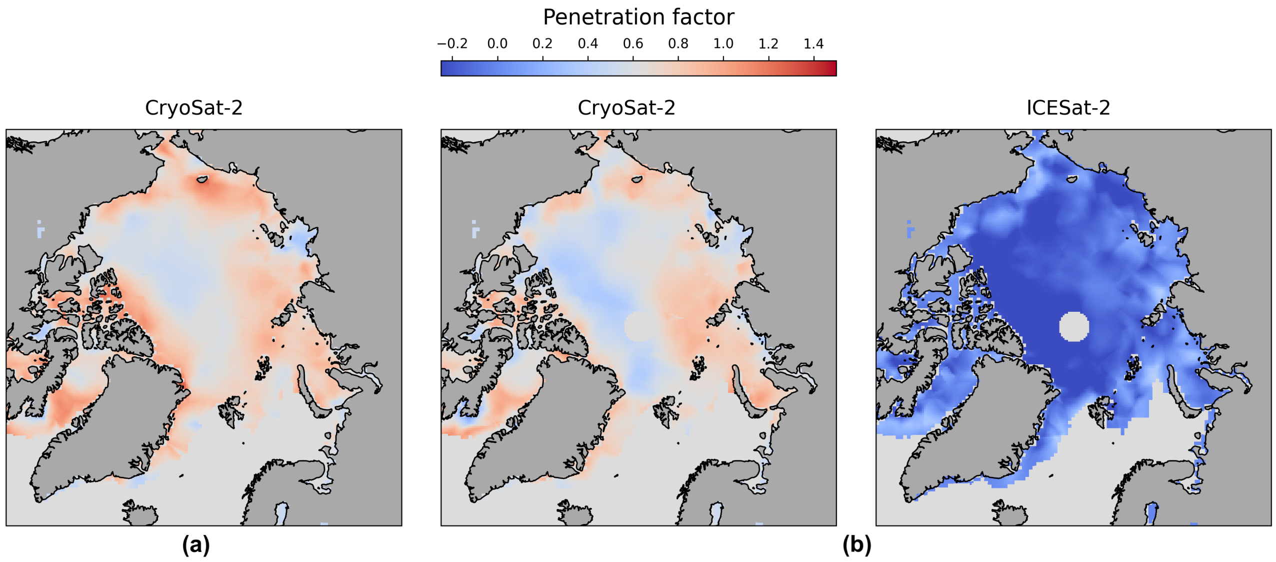

Figure 12. Result of the inversion with (a) CS-IS-3p (inversion for SD, SIT and α_{cs}) and (b) CS-IS-4p (inversion for SD, SIT, α_{cs} and α_{is}) for April 2019 for the penetration factors. The priors on the different physical parameters can be found in Section 3.

Compared to OIB (Figure 9.(b)), the CS-IS-4p SD is statistically better than the SD computed with CS-IS-3p and than the SD used by the AWI product (see Table 2). The comparison for the SIT (bottom right of the figure) shows good performance for the slope and r coefficient. However, the bias and RMSE are very poor compared to AWI SIT product. Similar to the CS-IS-3p, the inversion with CS-IS-4p overestimates the SD and underestimates the SIT.

For April 2019, the pan-Arctic average of the penetration factors are $\alpha_{is,4p,average} = -0.094$, $\alpha_{cs,4p,average} = 0.66$ and $\alpha_{cs,3p,average} = 0.73$ (higher value than for April 2021, see Figure 8).

Again, we evaluate the performance of the inverse SD to MOSAiC and IceBird SD products on Figure 13. We retrieve similar results than with CS-IS-3p (see Figure 10) for the validation against MOSAiC. Indeed, the slope, intercept, bias and RMSE are close. We plot on Figure 14 the average values for α_{cs} and α_{is}. Same as before, the region covered by MOSAiC is a region with lower α_{cs} (around 0.5 - 0.6). This region is also characterized by negative values for α_{is} (around -0.25).

The evaluation against IceBird is again more promising with a slope close to 1 and low values for Bias and RMSE (0.04 and 0.08 respectively). The intercept is also close to 1 (0.05). Thanks to Figure 12, these are (as for CS-IS-3p) regions of higher values for α_{cs} (especially over the North of Greenland). Over these regions of comparison with IceBird, the penetration factor for IS is very negative (α_{cs} < - 0.2).

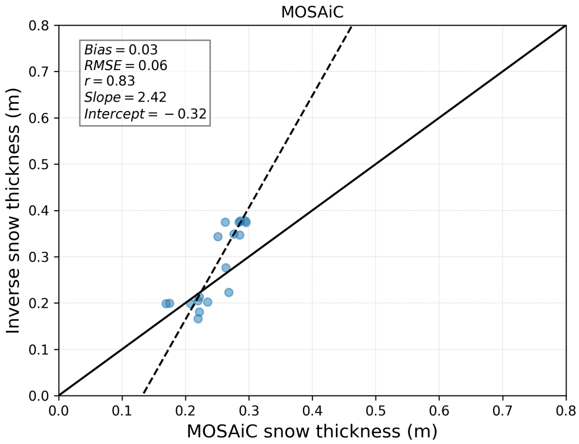

Figure 13. Evaluation of the results from the inversion using CS-IS-4p for SD. The validation is performed against MOSAiC (for Winter 2019-2020) and IceBird (for 2019/04).

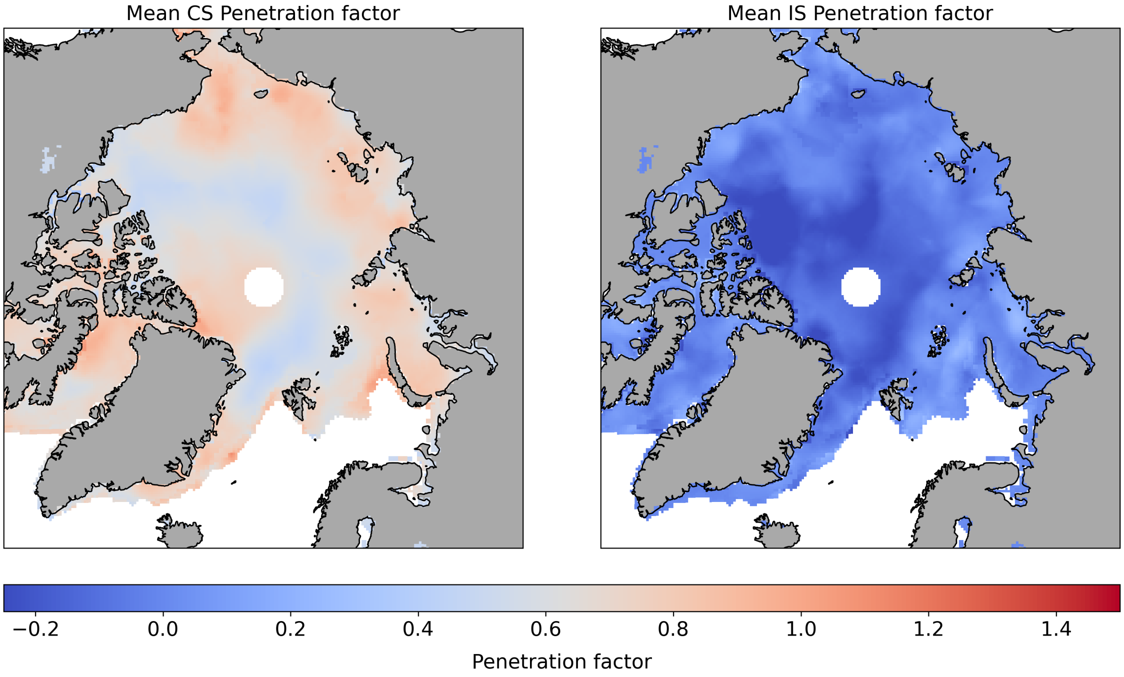

Figure 14. Average penetration factors for (left) CryoSat-2 and (right) ICESat-2, for Winter 2019-2020, computed with CS-IS-4p.

https://doi.org/10.5194/egusphere-2025-1163
Preprint. Discussion started: 28 April 2025

5 Discussion

5.1 Sea ice thickness and snow depth retrievals

This study demonstrates the capability of the Bayesian approach to simultaneously retrieve SIT and SD from along-track freeboard measurements, without requiring data interpolation or coincident satellite orbits. The methodology successfully captures well-established geographical patterns in SIT and SD, including the presence of thicker ice north of Greenland and within the Canadian Archipelago, regions dominated by MYI.

The retrieved SIT and SD estimates show promising agreement with existing datasets, exhibiting consistency with AWI SIT and AMSR2 SD products. Furthermore, the results display strong correlations with validation data (OIB, MOSAiC, IceBird), as illustrated in Figures 3, 5, and 6. However, a systematic bias is observed, with the inversion method underestimating SIT by 0.18 m while overestimating SD by 0.15 m relative to OIB. Several potential explanations for this bias are considered. One contributing factor may be the assumption of full radar penetration in the CryoSat-2 retrievals ($\alpha_{cs} = 1$). Differentiating the freeboard equations (Equations 3, 5) with respect to α_{cs} indicates that an increase in penetration factor ($\alpha_{cs} > 1$) would lead to higher SIT estimates. However, given that penetration factors are typically constrained within the range [0,1], a value exceeding unity would suggest scattering of the Ku-band within the ice pack, which is not physically expected. Additionally, the observed 18 cm SIT underestimation could be linked to systematic biases in the input freeboard data or the smoothing effect of the inversion approach over the OIB comparison region (left map in Figure 3).

Regarding SD retrieval, the overestimation of 0.15 m compared to OIB aligns with known biases in the OIB Quick-Look SD product, which underestimates SD by approximately 0.08 m (Kwok et al., 2017). When evaluating SD inversion performance against MOSAiC (Winter 2019-2020) and IceBird (April 2019), different trends emerge. The CS-IS-2p inversion underestimates SD by 0.19 m compared to MOSAiC. This discrepancy compared to the OIB evaluation may be attributed to period and regional differences, as MOSAiC measurements were conducted during Winter 2019-2020 in the central Arctic, north of Svalbard, whereas OIB data correspond to April 2019 observations with measurements made in other regions of Central Arctic. For IceBird, where the meaurements were also performed during April 2019, the inversion yields an SD overestimation of 0.03 m, suggesting a closer agreement with OIB than with MOSAiC. The differences in measurement techniques and geographical coverage likely explain the varying correlation statistics observed across validation datasets (OIB, MOSAiC and IceBird).

For CS-IS-3p and CS-IS-4p (Figures 9, 10, 13), the results are also promising in some cases (OIB SIT and IceBird SD) but some tuning of the parameters is needed to obtain better correlations (especially for the evaluation against OIB and MOSAiC SD). For these two inversions (CS-IS-3p, CS-IS-4p), the algorithm still underestimates the SIT compared to OIB (Figure 9). This underestimation is significantly larger than that obtained with CS-IS-2p, with values of 2.15 m for CS-IS-3p and 0.66 m for CS-IS-4p. According to Equations 3, 5, assuming a prescribed value of α_{is} = 0, an increase in α_{cs} leads to an increase in SIT. As shown in Figure 10, for both CS-IS-3p and CS- IS-4p, α_{cs} remains close to or below unity in the region used for comparison with OIB (see map in Figure 3). Consequently, the greater underestimation of SIT observed with CS-IS-3p and CS-IS-4p compared to CS-IS-2p is consistent with these findings.

5.2 Computation of penetration factors in addition to SIT and SD

Given an user-defined prior probability distribution $P(\mathbf{m})$, the inversion framework estimates the penetration factors for each satellite. The retrieved values align well with expected ranges for radar (Ku-band) and laser measurements, despite the use of a weakly constrained prior.

The method demonstrates robustness, as evidenced by the similar α_{cs} values obtained from the CS-IS-3p and CS-IS-4p inversions. For the CS-IS-3p model, the pan-Arctic average penetration factor is computed as 0.73 for April 2019 and 0.67 for April 2021. Notably, SIT is observed to be higher in April 2019 compared to April 2021, particularly in the region north of Greenland. Over the course of an entire winter, the CS-IS-3p inversion reveals a decreasing trend in α_{cs} (Figure 8), which corresponds to the observed increase in SD over the same period (Figure 7). As discussed in relation to the forward model equations (Section 3.1), this relationship is physically consistent, as thicker snow is expected to correspond to lower α_{cs} values.

The results for α_{is} obtained using the CS-IS-4p inversion exhibit predominantly negative values (Figure 12, 14). This suggests laser scattering occurring within the air above the snow layer. A possible explanation for this observation is the choice of the prior interval [-0.5, 0.5] for the IS penetration factor. However, it is noteworthy that the CS-IS-4p model performs slightly better than CS-IS-3p in terms of slope and intercept, while exhibiting a higher bias and RMSE when compared against OIB SIT and SD (Figure 9). Since the retrieved values for α_{cs} are similar in both models (Figure 12), it can be argued that the assumption of $\alpha_{is} = 0$ for the CS-IS-3p model may contribute to the increased bias observed in this last inversion. Nevertheless, the occurrence of negative IS penetration factor values remains an unexpected outcome that warrants further investigation.

These findings are promising and contribute to a better understanding of the behaviour of penetration factors and their influence on SIT and SD retrievals from freeboard measurements. Furthermore, this approach eliminates the need to assume fixed penetration factors when deriving SIT and SD, in contrast to previous studies (e.g. Kwok and Markus, 2017; Kwok et al., 2020; Kacimi and Kwok, 2022; Fredensborg Hansen et al., 2024). Further investigation is required to refine the spatial patterns observed in the retrieved penetration factor maps and their relationship with SIT and SD results. Adjustments to the prior distribution or modifications to the inversion framework may be necessary to ensure more physically consistent results (especially for α_{is}).

5.3 Forward modelling

In this study, we focused on 3 satellites (CS, IS, AK) but the method could be adapted to other radar/laser altimeters. In addition, we've only used a combination of two satellites. However, the algorithm can be easily modified to include freeboards from more than two satellites. This requires the definition of one equation per satellite (for example, we could perform the inversion with Equations 3, 4 and 5). The advantage of conducting the inversion using all three equations and satellites is that it leverages a larger dataset, enhancing the robustness of the analysis (3 data sources instead of 2). We could perform the inversion using a smaller number of days of data (e.g. 7 days) and still have the same number of freeboards as if we used two satellites but 15

https://doi.org/10.5194/egusphere-2025-1163
Preprint. Discussion started: 28 April 2025

days of data. This allowance for satellites fusion and the multiplicity of altimeters in orbit needs to be further investigated and is promising with a view to future missions.

We chose the snow density ρ_s to be spatially constant. The choice of the equation for the temporal variation of this density could also be refined (Mallet, 2024).

In an inverse problem, we need to define a forward model which is described by Equation 3, 4 and 5. These equations could be redefined to the extent that they are based on some assumptions (e.g hydrostatic equilibrium). A change in the forward modelling would have an impact on the inverse solution. Another idea would also be to invert for a *mass* $\frac{\rho_w - \rho_i}{\rho_w} H_i$ instead of inverting for SIT (c.f. Equation 3). This requires, of course, a choice on the prior for this new parameter.

Furthermore, while our study focuses on the Arctic, this algorithm can also be applied to estimate ice and snow thickness in the Antarctic. Additionally, the inversion can be performed over specific polar regions to enable targeted studies of particular areas.

5.4 Choice of the error

The estimated error associated to the observations is an input parameter of the inversion that can be modified. We decided to present our result with an error computed using the freeboard products uncertainties. Another approach to this specific question would be to set up a hyper-parameter λ to scale data errors and to use a hierarchical Bayes approach, where this parameter is treated as an unknown in the inversion (Malinverno and Briggs, 2004; Hawkins et al., 2019a):

$$\sigma = \lambda \sigma_{data} \tag{11}$$

where σ is the standard deviation in Equation 10, λ the unknown hierarchical parameter and σ_{data} the error vector on the input prior to the inversion.

6 Conclusions

We have introduced a new application of a Bayesian method for retrieving ice and snow over the Arctic. We showed that this innovative approach is valid for computing SIT and SD without assumptions on the SD (the main source of uncertainties). The solution is probabilistic, making possible further investigations on the covariances and on the joint probabilities of ice and snow depth. We presented comparisons of the inverted SD and SIT maps against other products (AWI, AMSR2, OIB, UiT) and independent data (MOSAiC, IceBird) which show promising results, though further tuning of the algorithm is necessary to generate an operational product of jointly inverted SD and SIT. This includes a better understanding of the impact of the penetration factor on both ice and snow depth.

This algorithm is also able to compute maps for the penetration factors of the satellites used. This could help the understanding of the behaviour of α and its link with SIT and SD (using the covariances for example or with more sensitivity studies). In the meantime, this will allow further investigation on temporal and spatial variability of the penetration factor.

One of the main advantages of this code is that it can be extensively customized and further improved. The forward model could be refined to invert for ice mass instead of the SIT or to invert for a deviation to a background instead of looking at absolute of the physical parameters. The error on the input could be changed and could even be an unknown for the inversion. This list of further investigations of this method is of course not exhaustive and paves the way for future works in order of efficiently construct maps of ice and snow depth over the poles.

Code availability. The code used to perform the inversion and plot the figures can be found on :
https://github.com/Elierb/Bayesian-trans-dimensional-inversion-from-satellite-altimeters-for-Arctic-ice-and-snow-retrievals.git

Data availability. The ice type data is available at Aaboe et al. (2021). The OIB Quick-Look data is available at Kurtz et al. (2016). The gridded CS2 and AK radar freeboard data are available via Landy et al. (2024). The along-track IS2 laser freeboard data is available at Kwok et al. (2023a). The AWI and AMSR-2 SIT products are available via Hendricks et al. (2023) and Rostosky et al. (2018) respectively. MOSAiC data are available via Itkin et al. (2021) and IceBird data can be found via Jutila et al. (2021).

Author contributions. ERB and MT led the project and the conceptualization of the study. ERB performed the inversions. ERB wrote the paper with the help of MT, TB, CN, SSBAR, JL, HH, RW and MF. CN and JL computed the along-track binned data and made the calculations of the uncertainties. TB and MF provided a theoretical support on the application of the method. SSBAR, JPF and TS worked on the development of the method. MT, CG and HH initiated the project several years ago.

Competing interests. Some authors are members of the editorial board of The Cryosphere

Acknowledgements. MT acknowledges support from ESA (#ESA/AO/1-9132/17/NL/MP & #ESA/AO/1-10061/19/I-EF, SINX'S, CLEV2ER) and NERC (#NE/T000546/1 & #NE/X004643/1). CN acknowledges support from NERC (#NE/S007229/1), the UK Met Office (CASE Partnership) and ESA (#ESA/AO/1-10061/19/I-EF).

References

Aaboe, S., Down, E., Sørensen, A., Lavergne, T., and Eastwood, S.: Sea-ice type climate data record Oct 1978-Aug 2023, https://doi.org/10.24381/CDS.29C46D83, 2021.

Alexandrov, V., Sandven, S., Wahlin, J., and Johannessen, O. M.: The relation between sea ice thickness and freeboard in the Arctic., The Cryosphere, 4(3), https://doi.org/10.5194/tc-4-373-2010, 2010.

Bodin, T. and Sambridge, M.: Seismic tomography with the reversible jump algorithm, Geophysical Journal International, 178, 1411–1436, https://doi.org/https://doi.org/10.1111/j.1365-246X.2009.04226.x, 2009.

Brodzik, M. J., Billingsley, B., Haran, T., Raup, B., and Savoie, M. H.: EASE-grid 2.0: Incremental but significant improvements for Earth-gridded data sets., ISPRS International Journal of Geo-Information, https://doi.org/https://doi.org/10.3390/ijgi1010032, 2012.

Brooks, S., Gelman, A., Jones, G., and Meng, X.-L.: Handbook of Markov Chain Monte Carlo, New York: Chapman and Hall/CRC, 2011.

Dettmering, D., Schwatke, C., and Bosch, W.: Global Calibration of SARAL/AltiKa Using Multi-Mission Sea Surface Height Crossovers, Marine Geodesy, 38, 206–218, https://doi.org/https://doi.org/10.1080/01490419.2014.988832, 2015.

Forsström, S., Gerland, S., and Pedersen, C. A.: Annals of Glaciology, 52, 261–270, 2011.

Fredensborg Hansen, R. M., Skourup, H., Rinne, E., Høyland, K. V., Landy, J. C., Merkouriadi, I., and Forsberg, R.: Arctic Freeboard and Snow Depth From Near-Coincident CryoSat-2 and ICESat-2 (CRYO2ICE) Observations: A First Examination of Winter Sea Ice During 2020–2022, Earth and Space Science, 11, e2023EA003 313, https://doi.org/https://doi.org/10.1029/2023EA003313, 2024.

Giles, K., Laxon, S., Wingham, D., Wallis, D., Krabill, W., Leuschen, C., McAdoo, D., Manizade, S., and Raney, R.: Combined air-borne laser and radar altimeter measurements over the Fram Strait in May 2002, Remote Sensing of Environment, 111, 182–194, https://doi.org/https://doi.org/10.1016/j.rse.2007.02.037, 2007.

Green, P. J.: Reversible jump Markov chain Monte Carlo computation and Bayesian model determination, Biometrika, 82, 711–732, https://doi.org/https://doi.org/10.1093/biomet/82.4.711, 1995.

Gregory, W., Lawrence, I. R., and Tsamados, M.: A Bayesian approach towards daily pan-Arctic sea ice freeboard estimates from combined CryoSat-2 and Sentinel-3 satellite observations, The Cryosphere, https://doi.org/https://doi.org/10.5194/tc-15-2857-2021, 2021.

Gregory, W., Bushuk, M., Zhang, Y., Adcroft, A., and Zanna, L.: Machine Learning for Online Sea Ice Bias Correction Within Global Ice-Ocean Simulations, Geophysical Research Letters, 51, https://doi.org/https://doi.org/10.1029/2023GL106776, 2024.

Guerreiro, K., Fleury, S., Zakharova, E., Rémy, F., and Kouraev, A.: Potential for estimation of snow depth on Arctic sea ice from CryoSat-2 and SARAL/AltiKa missions, Remote Sensing of Environment, 186, 339–349, https://doi.org/http://dx.doi.org/10.1016/j.rse.2016.07.013, 2016.

Hawkins, R., Bodin, T., Sambridge, M., Choblet, G., and Husson, L.: Trans-dimensional surface reconstruction with different classes of parameterization, Geochemistry, Geophysics, Geosystems, 20, 505–529, https://doi.org/https://doi.org/10.1029/2018GC008022, 2019a.

Hawkins, R., Husson, L., Choblet, G., Bodin, T., and Pfeffer, J.: Virtual tide gauges for predicting relative sea level rise, Journal of Geophysical Research: Solid Earth, 124, 13 367–13 391, https://doi.org/https://doi.org/10.1029/2019JB017943, 2019b.

Hendricks, S., Ricker, R., and Paul, S.: Product User Guide & Algorithm Specification: AWI CryoSat-2 Sea Ice Thickness (version 2.6), 2023.

Itkin, P., Webster, M., Hendricks, S., Oggier, M., Jaggi, M., Ricker, R., Arndt, S., Divine, D. V., von Albedyll, L., Raphael, I., Rohde, J., and Liston, G. E.: Magnaprobe snow and melt pond depth measurements from the 2019-2020 MOSAiC expedition, https://doi.org/10.1594/PANGAEA.937781, 2021.

Jutila, A., Hendricks, S., Ricker, R., von Albedyll, L., and Haas, C.: Airborne sea ice parameters during the IceBird Winter 2019 campaign in the Arctic Ocean, Version 1, https://doi.org/10.1594/PANGAEA.933912, 2021.

Kacimi, S. and Kwok, R.: Arctic Snow Depth, Ice Thickness, and Volume From ICESat-2 and CryoSat-2: 2018–2021, Geophysical Research Letters, 49, e2021GL097 448, https://doi.org/https://doi.org/10.1029/2021GL097448, 2022.

Kurtz, N., Studinger, M., Harbeck, J., Onana, V., and Yi, D.: IceBridge Sea Ice Freeboard, Snow Depth, and Thickness Quick Look, Version 1, https://doi.org/10.5067/GRIXZ91DE0L9, 2016.

Kwok, R.: Simulated effects of a snow layer on retrieval of CryoSat-2 sea ice freeboard, Geophysical Research Letters, 41, 5014–5020, https://doi.org/https://doi.org/10.1002/2014GL060993, 2014.

Kwok, R.: Arctic sea ice thickness, volume, and multiyear ice coverage: losses and coupled variability (1958–2018), Environmental Research Letters, 13, https://doi.org/DOI 10.1088/1748-9326/aae3ec, 2018.

Kwok, R. and Markus, T.: Potential basin-scale estimates of Arctic snow depth with sea ice freeboards from CryoSat-2 and ICESat-2: An exploratory analysis, Advances in Space Research, 62, https://doi.org/https://doi.org/10.1016/j.asr.2017.09.007, 2017.

Kwok, R. and Rothrock, D. A.: Decline in Arctic sea ice thickness from submarine and ICESat records: 1958–2008, Geophysical Research Letters, 36, https://doi.org/https://doi.org/10.1029/2009GL039035, 2009.

Kwok, R., Kurtz, N. T., Brucker, L., Ivanoff, A., Newman, T., Farrell, S. L., King, J., Howell, S., Webster, M. A., Paden, J., Leuschen, C., MacGregor, J. A., Richter-Menge, J., Harbeck, J., , and Tschudi, M.: Intercomparison of snow depth retrievals over Arctic sea ice from radar data acquired by Operation IceBridge, The Cryosphere, 11, 2571–2593, https://doi.org/https://doi.org/10.5194/tc-11-2571-2017, 2017.

Kwok, R., Kacimi, S., Webster, M., Kurtz, N., and Petty, A.: Arctic Snow Depth and Sea Ice Thickness From ICESat-2 and CryoSat-2 Freeboards: A First Examination, Journal of Geophysical Research: Oceans, 125, https://doi.org/https://doi.org/10.1029/2019JC016008, 2020.

Kwok, R., Petty, A., Cunningham, G., Markus, T., Ivanoff, D. H. A., Wimert, J., Bagnardi, M., and Kurtz, N.: ATLAS/ICESat-2 L3A Sea Ice Freeboard, Version 6, https://doi.org/10.5067/ATLAS/ATL10.006, 2023a.

Kwok, R., Petty, A. A., Cunningham, G., Markus, T., Hancock, D., I., A., W., J., B., M., K. N., and the ICESat-2 Science Team: (ATL10, Version 6), https://doi.org/https://doi.org/10.5067/ATLAS/ATL10.006, 2023b.

Landy, J. C., Petty, A. A., Tsamados, M., and Stroeve, J. C.: Sea ice roughness overlooked as a key source of uncertainty in CryoSat-2 ice freeboard retrievals, Journal of Geophysical Research: Oceans, 125, e2019JC015 820, 2020.

Landy, J. C., Dawson, G. J., Tsamados, M., Bushuk, M., Stroeve, J. C., Howell, S. E. L., Krumpen, T., Babb, D. G., Komarov, A. S., Heorton, H. D. B. S., Belter, H. J., and Aksenov, Y.: A year-round satellite sea-ice thickness record from CryoSat-2, Nature, 609, 517–522, https://doi.org/https://doi.org/10.1038/s41586-022-05058-5, 2022.

Landy, J. C., de Rijke-Thomas, C., Nab, C., Lawrence, I., Glissenaar, I. A., Mallett, R. D., Fredensborg Hansen, R. M., Petty, A., Tsamados, M., Macfarlane, A. R., et al.: Anticipating CRISTAL: An exploration of multi-frequency satellite altimeter snow depth estimates over Arctic sea ice, 2018–2023, EGUsphere, 2024, 1–41, https://doi.org/https://doi.org/10.5194/egusphere-2024-2904, 2024.

Lawrence, I. R., Tsamados, M. C., Stroeve, J. C., Armitage, T. W., and Ridout, A. L.: Estimating snow depth over Arctic sea ice from calibrated dual-frequency radar freeboards, The Cryosphere, 12, 3551–3564, https://doi.org/https://doi.org/10.5194/tc-12-3551-2018, 2018.

Laxon, S., Peacock, N., and Smith, D.: High interannual variability of sea ice thickness in the Arctic region, Nature, https://doi.org/https://doi.org/10.1038/nature02050, 2003.

Malinverno, A. and Briggs, V. A.: Expanded uncertainty quantification in inverse problems: Hierarchical Bayes and empirical Bayes, Geophysics, 69, https://doi.org/https://doi.org/10.1190/1.1778243, 2004.

Mallet, R.: A methodologically robust seasonal snow densification function from Soviet North Pole drifting station data, Manuscript submitted for publication, 2024.

Mallett, R. D., Lawrence, I. R., Stroeve, J. C., Landy, J. C., and Tsamados, M.: Brief communication: Conventional assumptions involving the speed of radar waves in snow introduce systematic underestimates to sea ice thickness and seasonal growth rate estimates, The Cryosphere, 14, 251–260, https://doi.org/10.5194/tc-14-251-2020, 2020.

Nab, C., Mallett, R., Gregory, W., Landy, J., Lawrence, I., Willatt, R., Stroeve, J., and Tsamados, M.: Synoptic variability in satellite altimeter-derived radar freeboard of Arctic sea ice, Geophysical Research Letters, 50, e2022GL100 696, https://doi.org/10.1029/2022GL100696, 2023.

Nab, C., Mallett, R., Nelson, C., Stroeve, J. C., and Tsamados, M.: Optimising interannual sea ice thickness variability retrieved from CryoSat-2, Geophysical Research Letters, p. e2024GL111071, https://doi.org/10.1029/2024GL111071, 2024.

Nab, C., Mignac, D., Landy, J., Martin, M., Stroeve, J., and Tsamados, M.: Sensitivity to sea ice thickness parameters in a coupled ice-ocean data assimilation system, Journal of Advances in Modeling Earth Systems, https://doi.org/10.1029/2024MS004276, 2025.

Nandan, V., Geldsetzer, T., Yackel, J., Mahmud, M., Scharien, R., Howell, S., King, J., Ricker, R., and Else, B.: Effect of Snow Salinity on CryoSat-2 Arctic First-Year Sea Ice Freeboard Measurements, Geophysical Research Letters, 44, https://doi.org/10.1002/2017GL074506, 2017.

Nicolaus, M., Perovich, D. K., Spreen, G., Granskog, M. A., von Albedyll, L., Angelopoulos, M., Anhaus, P., Arndt, S., Belter, H. J., Bessonov, V., Birnbaum, G., Brauchle, J., Calmer, R., Cardellach, E., Cheng, B., Clemens-Sewall, D., Dadic, R., Damm, E., de Boer, G., Demir, O., Dethloff, K., Divine, D. V., Fong, A. A., Fons, S., Frey, M. M., Fuchs, N., Gabarró, C., Gerland, S., Goessling, H. F., Gradinger, R., Haapala, J., Haas, C., Hamilton, J., Hannula, H.-R., Hendricks, S., Herber, A., Heuzé, C., Hoppmann, M., Høyland, K. V., Huntemann, M., Hutchings, J. K., Hwang, B., Itkin, P., Jacobi, H.-W., Jaggi, M., Jutila, A., Kaleschke, L., Katlein, C., Kolabutin, N., Krampe, D., Kristensen, S. S., Krumpen, T., Kurtz, N., Lampert, A., Lange, B. A., Lei, R., Light, B., Linhardt, F., Liston, G. E., Loose, B., Macfarlane, A. R., Mahmud, M., Matero, I. O., Maus, S., Morgenstern, A., Naderpour, R., Nandan, V., Niubom, A., Oggier, M., Oppelt, N., Pätzold, F., Perron, C., Petrovsky, T., Pirazzini, R., Polashenski, C., Rabe, B., Raphael, I. A., Regnery, J., Rex, M., Ricker, R., Riemann-Campe, K., Rinke, A., Rohde, J., Salganik, E., Scharien, R. K., Schiller, M., Schneebeli, M., Semmling, M., Shimanchuk, E., Shupe, M. D., Smith, M. M., Smolyanitsky, V., Sokolov, V., Stanton, T., Stroeve, J., Thielke, L., Timofeeva, A., Tonboe, R. T., Tavri, A., Tsamados, M., Wagner, D. N., Watkins, D., Webster, M., and Wendisch, M.: Overview of the MOSAiC expedition: Snow and sea ice, Elementa: Science of the Anthropocene, 10, 000 046, https://doi.org/10.1525/elementa.2021.000046, 2022.

Oelsmann, J., Marcos, M., Passaro, M., Sanchez, L., Dettmering, D., Dangendorf, S., and Seitz, F.: Regional variations in relative sea-level changes influenced by nonlinear vertical land motion, Nature Geoscience, 17, 137–144, https://doi.org/https://doi.org/10.1038/s41561-023-01357-2, 2024.

Petty, A. A., Keeney, N., Cabaj, A., Kushner, P., and Bagnardi, M.: Winter Arctic sea ice thickness from ICESat-2: upgrades to freeboard and snow loading estimates and an assessment of the first three winters of data collection, The Cryosphere, 17, 127–156, https://doi.org/https://doi.org/10.5194/tc-17-127-2023, 2023.

Pörtner, H.-O., Roberts, D., Masson-Delmotte, V., Zhai, P., Tignor, M., Poloczanska, E., Mintenbeck, K., Alegría, A., Nicolai, M., Okem, A., Petzold, J., Rama, B., and Weyer, N.: Summary for Policymakers, IPCC Special Report on the Ocean and Cryosphere in a Changing Climate, 2019.

Rostosky, P., Spreen, G., Farrell, S. L., Frost, T., Heygster, G., and Melsheimer, C.: Snow Depth Retrieval on Arctic Sea Ice From Passive Microwave Radiometers—Improvements and Extensions to Multiyear Ice Using Lower Frequencies, Journal of Geophysical Research: Oceans, 123, https://doi.org/https://doi.org/10.1029/2018JC014028, 2018.

Sambridge, M., Braun, J., and McQueen, H.: Geophysical parametrization and interpolation of irregular data using natural neighbours, Geophysical Journal International, 122, https://doi.org/https://doi.org/10.1111/j.1365-246X.1995.tb06841.x, 1995.

Shi, H., Sohn, B.-J., Dybkjær, G., Tonboe, R. T., and Lee, S.-M.: Simultaneous estimation of wintertime sea ice thickness and snow depth from space-borne freeboard measurements, The Cryosphere, https://doi.org/https://doi.org/10.5194/tc-14-3761-2020, 2020.

Stroeve, J. and Notz, D.: Changing state of Arctic sea ice across all seasons, Environmental Research Letters, 13, 103 001, https://doi.org/10.1088/1748-9326/aade56, 2018.

Tarantola, A.: Inverse problem theory and methods for model parameter estimation, 2005.

Tilling, R. L., Ridout, A., and Shepherd, A.: Estimating Arctic sea ice thickness and volume using CryoSat-2 radar altimeter data., Advances in Space Research, 62, https://doi.org/https://doi.org/10.1016/j.asr.2017.10.051, 2018.

Wadhams, P., Tucker, W. B., Krabill, W. B., Swift, R. N., Comiso, J. C., and Davis, N. R.: Relationship Between Sea Ice Freeboard and Draft in the Arctic Basin, and Implications for Ice Thickness Monitoring, Journal of Geophysical Research, 97, https://doi.org/https://doi.org/10.1029/92JC02014, 1992.

Warren, S. G., Rigor, I. G., Untersteiner, N., Radionov, V. F., Bryazgin, N. N., Aleksandrov, Y. I., and Colony, R.: Snow Depth on Arctic Sea Ice, Journal of Climate, 12, 1814 – 1829, https://doi.org/10.1175/15200442(1999)012<1814:SDOASI>2.0.CO;2, 1999.

Webster, M. A., Rigor, I. G., Nghiem, S. V., Kurtz, N. T., Farrell, S. L., Perovich, D. K., and Sturm, M.: Interdecadal changes in snow depth on Arctic sea ice, Journal of Geophysical Research : Oceans, https://doi.org/10.1002/2014JC009985, 2014.

Willatt, R., Laxon, S., Giles, K., Cullen, R., Haas, C., and Helm, V.: Ku-band radar penetration into snow cover on Arctic sea ice using airborne data, Annals of Glaciology, https://doi.org/10.3189/172756411795931589, 2011.

Willatt, R., Stroeve, J. C., Nandan, V., Newman, T., Mallett, R., Hendricks, S., Ricker, R., Mead, J., Itkin, P., Tonboe, R., Wagner, D. N., Spreen, G., Liston, G., Schneebeli, M., Krampe, D., Tsamados, M., Demir, O., Wilkinson, J., Jaggi, M., Zhou, L., Huntemann, M., Raphael, I. A., Jutila, A., and Oggier, M.: Retrieval of Snow Depth on Arctic Sea Ice From Surface-Based, Polarimetric, Dual-Frequency Radar Altimetry, Geophysical Research Letters, https://doi.org/https://doi.org/10.1029/2023GL104461, 2023.

Wingham, D. J., Francis, C. R., Baker, S. Bouzinac, C., Brockley, D., Cullen, R., De Chateau-Thierry, P., Laxon, S. W., Mallow, U., Mavrocordatos, C., Phalippou, L., Ratier, G., Rey, L., Rostan, F., Viau, P., and Wallis, D. W.: CryoSat: A mission to determine the fluctuations in Earth's land and marine ice fields, Advances in Space Research, 37, 841–871, https://doi.org/https://doi.org/10.1016/j.asr.2005.07.027, 2006.

Zygmuntowska, M., Rampal, P., Ivanova, N., and Smedsrud, L. H.: Uncertainties in Arctic sea ice thickness and volume: new estimates and implications for trends, The Cryosphere, 8, 705–720, https://doi.org/https://doi.org/10.5194/tc-8-705-2014, 2014.